



Search for Higgs boson production in dilepton plus missing transverse energy final states with 8.1 fb^{-1} of $p\bar{p}$ collisions at $\sqrt{s} = 1.96 \text{ TeV}$

The DØ Collaboration

We present a search for the standard model Higgs boson in dilepton events with large missing transverse energy using 8.1 fb^{-1} of $p\bar{p}$ collisions at $\sqrt{s} = 1.96 \text{ TeV}$, collected with the DØ detector at the Fermilab Tevatron collider. Three leptonic states $e^{\pm}\mu^{\mp}$, $e^{+}e^{-}$ and $\mu^{+}\mu^{-}$ are considered. No significant excess above the standard model background expectation is observed, and upper limits on Higgs boson production are derived, which exclude at 95% CL a standard model Higgs boson with a mass of $M_H = 165 \text{ GeV}$. Assuming the presence of a fourth generation of fermions with large masses, we exclude a SM-like Higgs with a mass between 140 and 240 GeV.

Preliminary Results for Summer Conferences 2011

I. INTRODUCTION

In the standard model (SM) the masses of the charged fermions are generated by their interaction with a scalar field, the Higgs boson, which has yet to be discovered. The Higgs boson is the residual degree of freedom after the spontaneous symmetry breaking of the electroweak gauge symmetry $SU(2) \otimes U(1)$ which is responsible for the generation of the masses of the W and Z bosons. Direct searches at the CERN e^+e^- collider (LEP) yield a lower limit for the SM Higgs boson mass, $M_H > 114.4$ GeV [1] at 95% confidence level (CL). A combination of results from the CDF and DØ experiments excludes the SM Higgs boson in the mass range $158 < M_H < 173$ GeV at 95% CL [2]. Indirect constraints from fits to precision electroweak measurements give an upper bound of $M_H < 185$ GeV [3] at 95% CL when combined with the direct searches from LEP2.

In this note, we present a search for the Higgs boson in states containing two leptons ($e^\pm\mu^\mp$, e^+e^- or $\mu^+\mu^-$) and missing transverse energy (\cancel{E}_T), using 8.1 fb^{-1} of $p\bar{p}$ collisions collected with the DØ detector at the Fermilab Tevatron. The combination of these final states has been shown to be most sensitive to a SM Higgs boson of mass $M_H \sim 160$ GeV [4].

The production of Higgs bosons by gluon fusion is considered, with the subsequent decay $H \rightarrow WW \rightarrow \ell\nu\ell'\nu'$, where the ℓ and ℓ' include muons and electrons, as well as τ leptons which themselves decay to muons or electrons. The contribution to the $e\mu$, ee , and $\mu\mu$ final state from weak vector boson fusion (VBF) and Higgs production in association with a vector boson (WH or ZH) is also considered, excluding events which are already considered in analyses targeting these specific processes. The preselection, based on the efficient reconstruction of the two leptons, is followed by additional requirements which suppress the large Drell-Yan (DY) $Z/\gamma^* \rightarrow \ell\ell$ background. A final multivariate analysis based on a random forest of decision trees (BDT) is used to separate the signal from the remaining background. The output of the BDT is the final discriminant used to search for the Higgs signal.

II. DØ DETECTOR

This analysis relies upon the efficient identification of muons, electrons, jets and missing transverse energy using the many subsystems of the DØ Run II detector [5]. The central tracking system consists of a silicon microstrip tracker (SMT) and a central fiber tracker (CFT), both located within a 2 T axial magnetic field. The SMT strips have a typical pitch of 50–80 μm , and the design is optimized for tracking and vertexing over the pseudorapidity range $|\eta| < 3$, where $\eta = -\ln(\tan\theta/2)$ with θ being the polar angle relative to the proton beam direction. The system has a six-barrel longitudinal structure, with each barrel a set of four silicon layers arranged axially around the beam pipe, interspersed with sixteen radial disks. In addition, a new layer of silicon (Layer 0) was added just outside the beam pipe in 2006. The upgrades to the detector and accelerator at this time marked the end of Run IIa and the beginning of Run IIb. The CFT has eight thin coaxial barrels, each supporting two doublets of overlapping scintillating fibers of 0.835 mm diameter, one doublet parallel to the beam axis, the other alternating by $\pm 3^\circ$ relative to the beam axis.

A liquid-argon/uranium calorimeter surrounds the central tracking system and consists of a central calorimeter (CC) covering to $|\eta| \approx 1.1$, and two end calorimeters (EC) extending coverage for $|\eta| < 4.2$, each housed in separate cryostats. Scintillators between the CC and EC cryostats provide sampling of showers for $1.1 < |\eta| < 1.4$.

The muon system is located outside the calorimeters and consists of a layer of tracking detectors and scintillation trigger counters inside toroid magnets which provide a 1.8 T magnetic field, followed by two similar layers behind each toroid. Tracking in the muon system for $|\eta| < 1$ relies on 10 cm wide drift tubes, while 1 cm mini-drift tubes are used for $1 < |\eta| < 2$. The numbers of hits in the wire chambers and in the scintillators of the muon spectrometer are combined to define a muon quality variable, used in the final stage of the analysis.

Trigger and data acquisition systems are designed to accommodate the high luminosities of Run II. Based on preliminary information from tracking, calorimetry, and muon systems, the output of the first level of the trigger is used to limit the rate for accepted events to ≈ 1.5 kHz. At the next trigger stage, with more refined information, the rate is reduced further to ≈ 0.8 kHz. These first two levels of triggering rely mainly on hardware and firmware. The third and final level of the trigger, with access to all the event information, uses software algorithms and a computing farm, and reduces the output rate to ≈ 100 Hz, which is written to tape.

III. DATA AND MONTE CARLO SAMPLES

The data sample used in this analysis was collected between April 2002 and December 2010 (Run II) by the DØ detector at the Fermilab Tevatron collider at $\sqrt{s} = 1.96$ TeV, and corresponds to an integrated luminosity of 8.1 fb^{-1} for the dilepton final state after imposing data quality requirements. The Run IIa dataset (1.1 fb^{-1}) and the

Run IIb dataset (7.0fb^{-1}) are analyzed separately. The luminosity is measured with an accuracy of 6.1% using plastic scintillator arrays located in front of the EC cryostats, covering $2.7 < |\eta| < 4.4$ [6].

Signal and SM background processes are simulated with PYTHIA [7] or ALPGEN [8] using the CTEQ6L1 [9] parton distribution functions (PDF), followed by a detailed GEANT-based [10] simulation of the DØ detector. In order to model the effects of multiple $p\bar{p}$ interactions, the MC samples are overlaid with events from random $p\bar{p}$ collisions with similar luminosity profiles and then reconstructed with the same software as the data. The normalization of the generated samples is scaled to match the highest-order cross section calculation available. For the gluon fusion $gg \rightarrow H$ process, the cross-section is calculated at NNLO+NNLL level [11], for WH and ZH at NNLO [12], and for vector boson fusion at NNLO in QCD [13]. All signal cross sections are computed using the MSTW 2008 NNLO PDF set [14]. The PDF uncertainties are assessed according to the recommendations of Ref. [15]. The distribution of the transverse momentum of the Higgs boson generated in the gluon fusion process is tuned to match the transverse momentum as calculated by HqT, at NNLL and NNLO accuracy [16].

The main background processes for this analysis are diboson production, Z/γ^* production in leptonic final states, electroweak W +jets/ γ production, $t\bar{t}$ production and multijet production with jets misidentified as leptons. For the W +jets and Z +jets backgrounds we use the ALPGEN [8] event generator. The background MC samples for inclusive W and Z production are normalized using the NNLO cross sections calculations of Ref. [17] using the NLO CTEQ 6.1 PDF. The Z boson p_T distribution is modeled to match the distribution observed in data [18], taking also into account the dependence on the number of reconstructed jets. To reproduce the W p_T distribution in simulated events, the product of the measured Z boson p_T spectrum in Ref. [18] multiplied by the ratio of W to Z boson p_T distributions at NLO from Ref. [19] is used to reweight events. In the ee and $e\mu$ channels, the W +jets sample includes contributions from events where a fake electron originates from a jet or a photon. The size of each of these contributions is corrected such that the distribution of the number of hits in the innermost silicon layer matches that observed in a W +jets enhanced control sample. The NNLO calculations of Ref. [20] are used for $t\bar{t}$ production, while the NLO WW , WZ and ZZ production cross section values are taken from Ref. [21]. For the main source of background, WW production, the p_T of the diboson system is modeled using the MC@NLO simulation [22] and the distribution of the opening angle of the two leptons is corrected to take into account the contribution from gluon fusion [23].

The background due to multi-jet production, where jets are misidentified as leptons, is determined from data. In order to obtain a high-statistics sample of predominantly multijet events the lepton quality requirements in each channel are inverted. To scale the multijet sample to the actual multijet contribution in the signal region, and to correct for kinematic bias from reversing the lepton quality requirements, the multijet sample is compared to events which pass all of the signal requirements except that the leptons have the same-sign. As the probability of a jet faking a lepton is independent of charge assuming small charge correlation between the leptons in multijet events, the same-sign sample has the exact same normalization and kinematics as the actual multijet contribution.

IV. PRESELECTION

All events satisfying any trigger of the DØ trigger suite are accepted for this analysis. While most events selected in the analysis are triggered by single-lepton and dilepton triggers, additional acceptance is gained by including triggers with jets or missing transverse energy. The simulated background samples are normalized to the integrated luminosity and cross section. An additional correction is required to normalize the Monte Carlo to match the data. This correction is determined in a Drell-Yan dominated sample and is smaller than the luminosity uncertainty.

In the offline analysis, electrons are identified using calorimeter and tracking information. Electromagnetic showers are identified in the calorimeter by comparing the longitudinal and transverse shower profiles to those of simulated electrons. The showers must be isolated, deposit 90% of their energy in the electromagnetic part of the calorimeter and pass a likelihood criterion that includes a spatial track match and, in the central detector region, an E/p requirement, where E is the energy of the calorimeter cluster and p is the momentum of the track. The value of the likelihood variable is referred to as the electron quality. Electrons are required to be in the acceptance of the calorimeter ($|\eta| < 1.1$ or $1.5 < |\eta| < 2.5$). In the dielectron channel, electrons reconstructed in the inter-cryostat region are not considered, and events with one electron in the end-cap calorimeter are treated separately from events with both electrons in the central calorimeter. This improves the analysis sensitivity as the background composition is different in the two pseudorapidity regions. The events where both the electrons are in the end cap calorimeter are not considered in the analysis due to large background and a small signal contribution. The transverse momentum measurement of the electrons is based on calorimeter energy information.

Muon tracks are reconstructed from hits in the wire chambers and scintillators in the muon system and must match a track in the central tracker. To select isolated muons, the scalar sum of the transverse momentum of all tracks, other than that of the muon, in a cone of $\mathcal{R} = 0.5$ around the muon track is calculated, where $\mathcal{R} = \sqrt{(\Delta\phi)^2 + (\Delta\eta)^2}$

and ϕ is the azimuthal angle. The transverse energy deposited in the calorimeter in a hollow cone of $0.1 < \mathcal{R} < 0.4$ around the muon is also measured. In the $e^\pm\mu^\mp$ final state, both quantities are required to be $< 0.15 \times p_T^\mu$, where p_T^μ is the transverse momentum of the muon. In the dimuon final state, the track isolation is required to be $< 0.25 \times p_T^\mu$ and the calorimeter isolation is required to be $< 0.4 \times p_T^\mu$. In addition, the calorimeter isolation for each muon is required to be less than 10 GeV. Muons are restricted to the fiducial coverage of the muon system $|\eta| < 2.0$. Muons from cosmic rays are rejected by requiring a timing criterion on the hits in the scintillator layers as well as applying restrictions on the position of the muon track with respect to the selected $p\bar{p}$ interaction vertex (primary vertex).

Hadronic jets are reconstructed from energy deposits in the calorimeter towers using an iterative midpoint cone algorithm with a cone radius of 0.5 [24]. All calorimeter jets are required to pass a set of quality criteria which are approximately 98% efficient and have at least two reconstructed tracks within $\Delta R(\text{track}, \text{jet-axis}) \leq 0.5$. Jets are also required to be consistent with originating from the $p\bar{p}$ interaction vertex.

The missing transverse energy, \cancel{E}_T , is obtained from a vector sum of transverse components of calorimeter energy depositions and corrected for identified muons. The jet energies are calibrated using transverse momentum balance in photon+jet events [25], and the correction is propagated to the \cancel{E}_T .

We select events where the two leptons with highest p_T (ℓ_1 and ℓ_2) have opposite charge and originate from the same position (within 2 cm) along the beamline; any additional reconstructed lepton is not considered. The requirements on the transverse momenta of the two leptons are the following: in the e^+e^- and $\mu^+\mu^-$ channels we select $p_T^{\ell_1} > 15$ GeV and $p_T^{\ell_2} > 10$ GeV, while in the $e^\pm\mu^\mp$ channel we select $p_T^\mu > 10$ GeV and $p_T^e > 15$ GeV. In addition, the dilepton invariant mass is required to exceed 15 GeV in all channels. This stage of the analysis is referred to as “preselection”. Figures 1-3 show several kinematic distributions from each dilepton channel at preselection. The transverse mass is defined as $M_T = \sqrt{2 \cdot p_T^\ell \cdot \cancel{E}_T \cdot (1 - \cos \Delta\phi(\ell, \cancel{E}_T))}$ and consequently the minimal transverse mass is $M_T^{\min} = \min(M_T^{\ell_1}, M_T^{\ell_2})$.

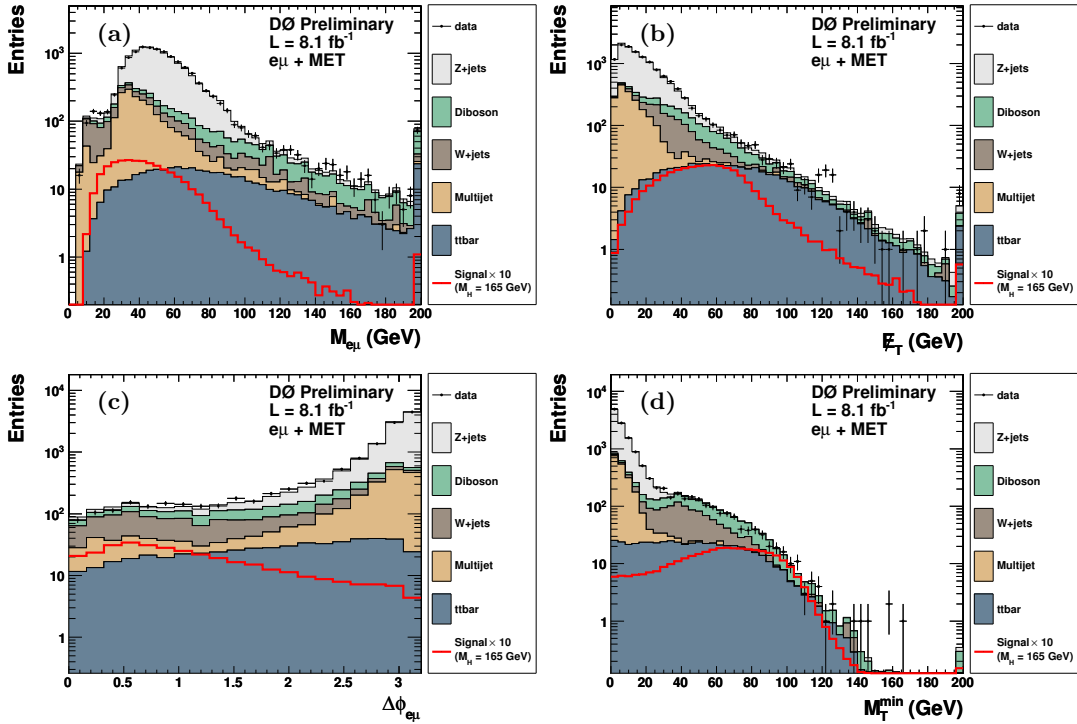


FIG. 1: The (a) dilepton mass, (b) \cancel{E}_T , (c) $\Delta\phi$ between the leptons, and (d) minimum transverse mass between either lepton and the \cancel{E}_T , for the $e\mu$ channel at the preselection stage. The highest bin includes all events above the upper range of the histogram (a,b,d).

In order to improve the sensitivity of the analysis in each dilepton channel, the preselection sample is further subdivided by the number of jets present in the event. Jets are required to have $E_T > 20$ GeV, $|\eta| < 2.4$, pass quality requirements, and to have charged tracks associated with the primary $p\bar{p}$ vertex. The subsequent analysis steps are then carried out separately for events with zero jets, one jet, and two or more jets, resulting in a total of nine analysis channels (three lepton channels each with three jet bins). Dividing the analysis into different jet bins significantly

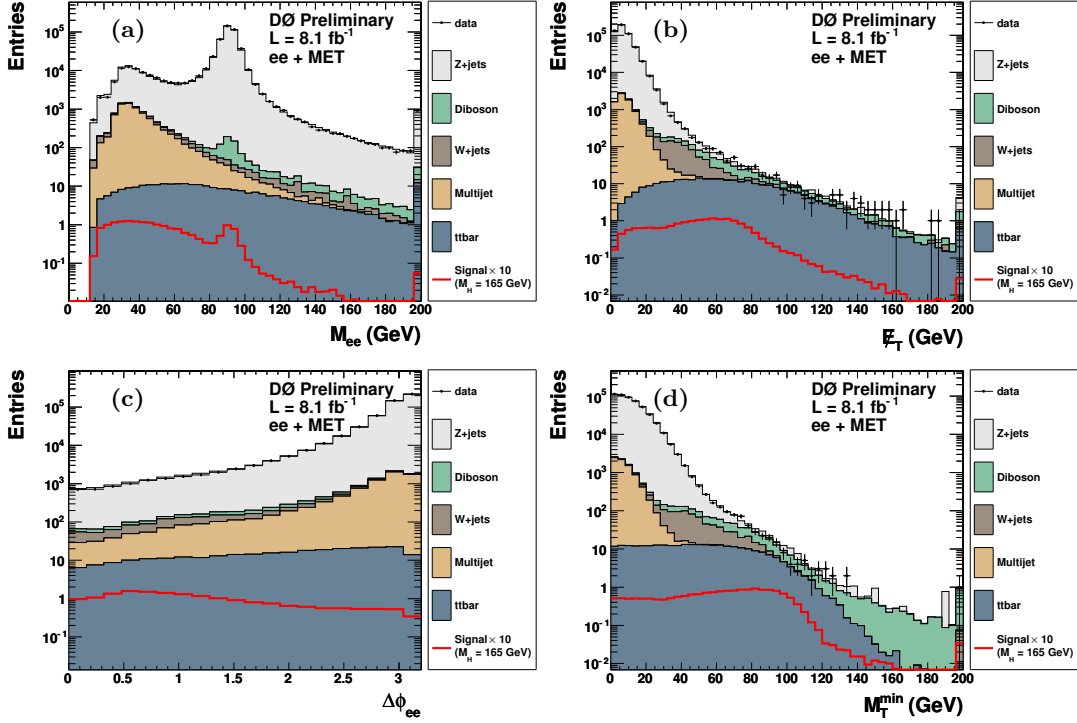


FIG. 2: The (a) dilepton mass, (b) E_T , (c) $\Delta\phi$ between the leptons, and (d) minimum transverse mass between either lepton and the E_T , for the ee channel at the preselection stage. The highest bin includes all events above the upper range of the histogram (a,b,d).

TABLE I: Expected and observed number of events for each jet multiplicity bin at preselection in the $e\mu$, ee and $\mu\mu$ final states. The signal assumes a Higgs boson mass of 165 GeV for each jet bin.

	Data	Total	Background	Signal	$Z \rightarrow ee$	$Z \rightarrow \mu\mu$	$Z \rightarrow \tau\tau$	$t\bar{t}$	W+jets	Diboson	Multi-jet
<i>$e\mu$:</i>											
0 jets	8505	8565.6	16.9	219.2	666.9	5292.6	17.5	613.6	604.6	1151.2	
1 jet	1396	1421.7	8.2	30.6	93.9	660.0	140.3	126.7	93.3	276.7	
≥ 2 jets	512	509.5	3.9	5.1	19.6	119.0	284.9	34.4	16.2	30.4	
<i>ee:</i>											
0 jets	447698	444084.1	8.4	433776.7	-	3820.1	11.2	658.7	448.2	5369.2	
1 jet	59806	60218.6	5.2	57115.0	-	645.2	88.8	184.5	201.9	1983.4	
≥ 2 jets	9352	9385.3	3.6	8622.1	-	111.1	189.0	22.1	154.6	286.5	
<i>$\mu\mu$:</i>											
0 jets	592539	598085.0	11.3	-	590715.5	4995.3	9.5	296.9	597.6	1470.2	
1 jet	79759	81791.7	6.9	-	80333.2	696.4	95.6	59.2	260.8	346.6	
≥ 2 jets	13574	14219.1	5.8	-	13521.4	117.8	258.3	11.4	222.2	87.9	

increases the sensitivity of this search as the signal and background composition change considerably between each sample.

The number of events in each jet multiplicity bin at preselection can be found in Table I. In general, good agreement between data and the expected background contribution is observed. At the preselection, the Z/γ^* contribution and multi-jet events are the dominant background sources.

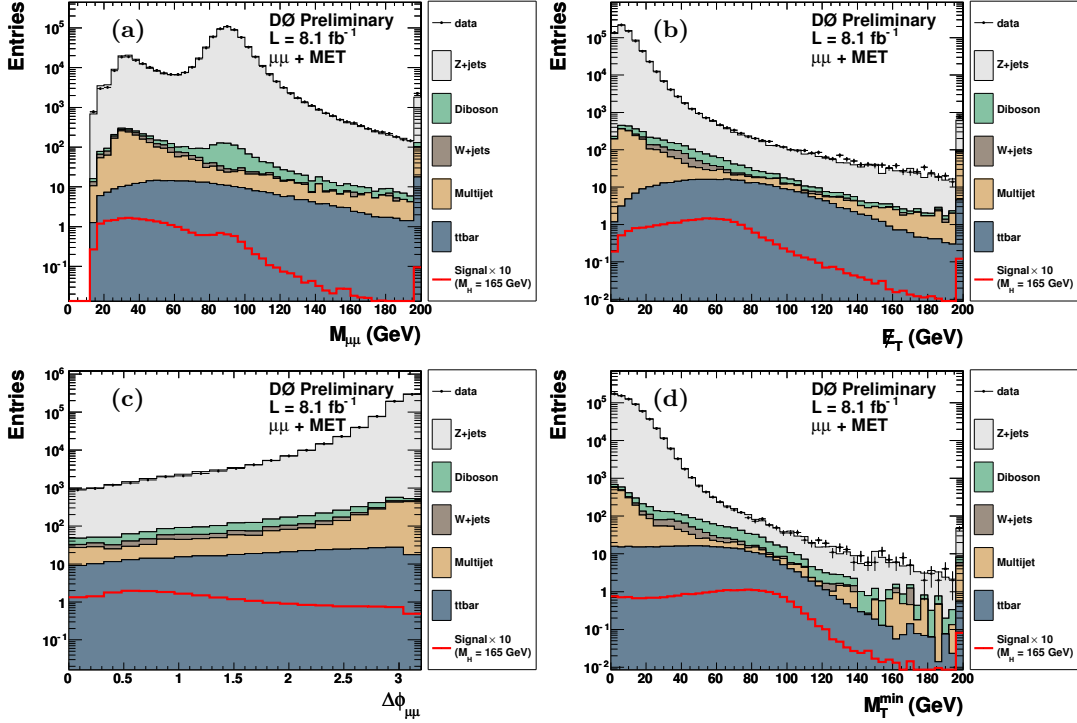


FIG. 3: The (a) dilepton mass, (b) E_T , (c) $\Delta\phi$ between the leptons, and (d) minimum transverse mass between either lepton and the E_T , for the $\mu\mu$ channel at the preselection stage. The highest bin includes all events above the upper range of the histogram (a,b,d).

V. FINAL SELECTION

The dielectron and dimuon channels use a random forest BDT discriminant to remove the dominant Z/γ^* background at the preselection (DY BDT). The BDT was trained for each Higgs mass point considered in each jet bin separately for dielectron and dimuon channels. The output of the BDT is a single number, which characterizes the event as background-like or signal-like.

The following list of input variables were used for the 0-jet DY BDT:

- p_T of ℓ_1 ;
- p_T of ℓ_2 ;
- invariant mass of the two leptons;
- azimuthal opening angle between the two leptons, $\Delta\phi(\ell, \ell)$;
- opening angle in η and ϕ space between the two leptons, $\Delta R(\ell, \ell)$;
- E_T ;
- E_T^{special} , where $E_T^{\text{special}} = E_T$ if $\Delta\phi(E_T, \text{nearest lepton or jet}) > \pi/2$ or $E_T^{\text{special}} = E_T \times \sin(\Delta\phi(E_T, \text{nearest lepton or jet}))$ otherwise;
- minimum transverse mass: $m_T^{\min} = \min\{m_T(\ell_1, E_T), m_T(\ell_2, E_T)\}$;
- minimum of azimuthal angle between E_T and each lepton;
- maximum of azimuthal angle between E_T and each lepton;
- transverse mass between E_T and dilepton pair, $M_T(\ell\ell, E_T)$;

- the M_{T2} variable, an extension of the transverse mass to final state with two visible and two invisible particles [26];

The 1-jet DY-BDT uses all of the variables for the 0-jet DY-BDT and the following additional variables:

- $\cancel{E}_T^{\text{Scaled}} = \cancel{E}_T / \sqrt{\sum_{\text{jets}} (\Delta E^{\text{jet}} \cdot \sin \theta^{\text{jet}} \cdot \cos \Delta \phi(\text{jet}, \cancel{E}_T))^2}$;
- jet p_T ;
- azimuthal angle between \cancel{E}_T and the jet;

The 2-jet DY-BDT uses all of the variables for the 0-jet DY-BDT, plus the 1-jet quantities with variables calculated for the two jets with highest- p_T (j_1 and j_2), and the following additional variables:

- absolute value of the rapidity difference between the jets, $\Delta \eta(j_1, j_2)$;
- invariant mass of the two jet, $M(j_1, j_2)$;

To reject most of the Z/γ^* background, a requirement is applied on this discriminant. The choice of such a requirement varies for each Higgs mass point in each jet bin. The DY-BDT discriminant for a Higgs boson mass of 165 GeV can be found in Figure 4.

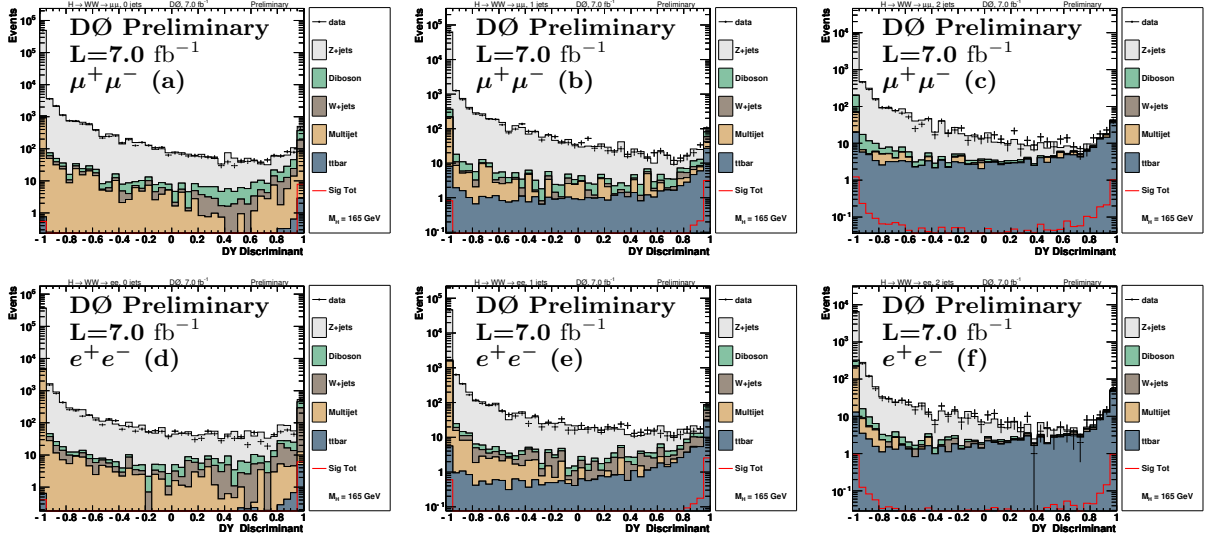


FIG. 4: DY BDT discriminant for $\mu\mu$ channel in (a) 0-jet bin, (b) 1-jet bin, (c) ≥ 2 -jet bin and same distributions for the ee channel in (c) 0-jet bin, (d) 1-jet bin and (e) ≥ 2 -jet bin; The discriminant shown is trained for a Higgs mass of 165 GeV. For the final selection a requirement at 0.9, -0.5 and -0.7 is applied in the above distributions for the 0-jet, 1-jet and ≥ 2 -jet bin respectively. These distributions correspond to the Run IIb dataset.

The $e^\pm\mu^\mp$ channel does not utilize a BDT discriminant to remove the Z/γ^* background, but instead applies kinematic based cuts to help reduce the dominant backgrounds after preselection. For the signal, large missing transverse energy is expected due to neutrinos in the final state. This is not the case for multi-jet and $Z/\gamma^* \rightarrow ee, \mu\mu$ events. In addition, the missing transverse energy is not expected to be aligned with any of the leptons for the signal while for Z/γ^* as well as multi-jet events this is the case. For the latter, the missing transverse energy is mostly caused by the mismeasured energy of fake leptons, thus the missing transverse energy tends to point in the direction of the fake leptons. For $Z/\gamma^* \rightarrow \tau\tau$ events, the charged leptons and the neutrinos follow the direction of the tau leptons due to the large boost, thus the missing transverse energy is also expected to be aligned with the leptons. A quantity that takes into account both the absolute value of the missing transverse energy as well as the angle to the leptons is the minimal transverse mass, $M_T^{\min} = \min(M_T^e, M_T^\mu)$, and is expected to peak at lower values for Z/γ^* and multi-jet events compared to the signal. Thus, the electron-muon final state requires the minimum transverse mass larger than 20 GeV and rejects the majority of these events. An additional requirement on $M_{T2} > 15$ GeV is also placed to further reduce these backgrounds. The distributions of M_T^{\min} and M_{T2} for the electron-muon final state at preselection are shown in Figure 5 for each jet multiplicity bin.

The numbers of events at the final selection for each of the dilepton states are shown in Table II.

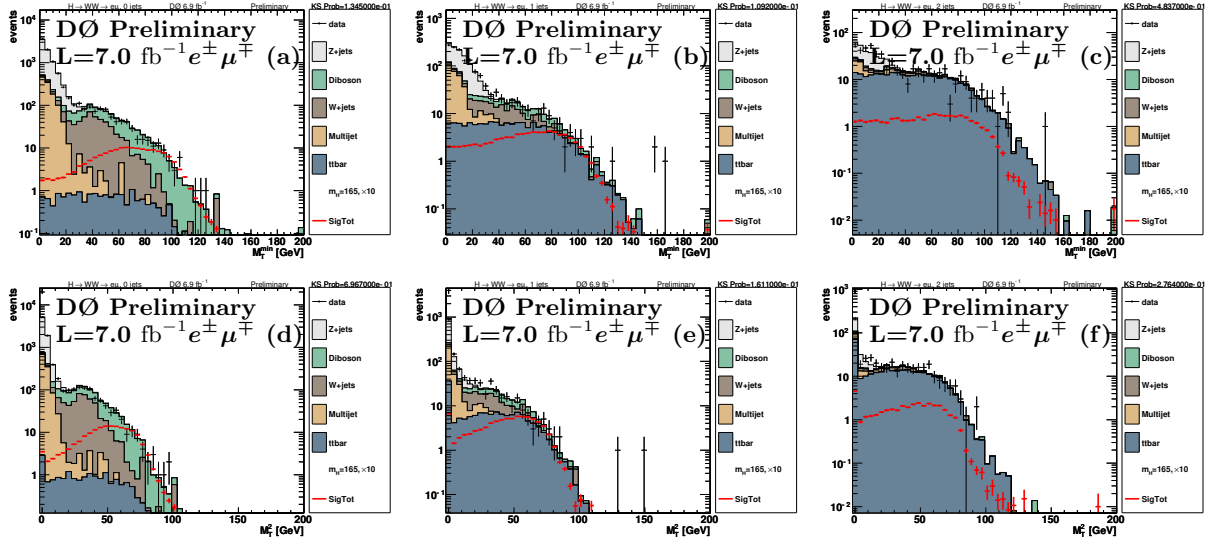


FIG. 5: M_T^{\min} distribution for the $e\mu$ channel in (a) 0-jet bin, (b) 1-jet bin, (c) ≥ 2 -jet bin. M_{T2} distribution for the $e\mu$ channel in (d) 0-jet bin, (e) 1-jet bin, (f) ≥ 2 -jet bin. For the final selection, a requirement of $M_T^{\min} > 20$ GeV and $M_{T2} > 15$ GeV is placed for all 3 jet multiplicity bins. These distributions correspond to the Run IIb dataset.

TABLE II: Expected and observed number of events for each jet multiplicity bin after the final selection in the $e\mu$, ee , and $\mu\mu$ final states. The signal assumes a Higgs boson mass of 165 GeV for each jet bin. The numbers in brackets correspond to the efficiency of the final selection with respect to the preselection, shown in Table I, for both the total background and signal.

	Data	Total Background	Signal	$Z \rightarrow ee$	$Z \rightarrow \mu\mu$	$Z \rightarrow \tau\tau$	$t\bar{t}$	W+jets	Diboson	Multi-jet
$e\mu$:										
0 jets	881	948.8 ± 118.6 (11.2%)	15.7 (92.9%)	3.3	39.3	6.5	12.2	436.0	435.9	15.7
1 jet	255	244.4 ± 38.4 (17.2%)	6.8 (82.9%)	2.0	9.0	2.0	86.7	76.6	55.6	12.6
≥ 2 jets	214	206.9 ± 30.0 (40.6%)	3.0 (76.9%)	0.7	2.3	0.60	174.5	21.0	7.7	0.11
ee :										
0 jets	676	715.8 ± 89.9 (0.2%)	7.2 (85.7%)	108.5	-	9.1	6.1	376.8	205.3	10.0
1 jet	836	831.9 ± 144.5 (1.4%)	4.2 (80.8%)	477.6	-	83.5	75.4	125.0	56.9	14.2
≥ 2 jets	477	442.6 ± 73.9 (4.7%)	2.4 (66.7%)	201.7	-	42.9	160.8	13.9	17.1	6.2
$\mu\mu$:										
0 jets	612	689.7 ± 60.7 (0.1%)	9.3 (82.3%)	-	201.8	2.7	3.8	136.6	240.6	104.2
1 jet	1420	1313.2 ± 173.3 (1.6%)	5.5 (79.7%)	-	969.1	109.8	76.4	38.0	74.4	45.6
≥ 2 jets	888	890.8 ± 135.4 (6.3%)	3.7 (63.8%)	-	579.6	46.8	209.4	7.2	28.2	19.5

VI. FINAL DISCRIMINANTS

At final selection, the signal is separated from the remaining background using an additional random forest decision tree (BDT). For the ee and $\mu\mu$ channels this two step approach allows the modeling of the smaller backgrounds to be investigated. The final discriminant BDT uses as inputs all the variables used for the DY discriminant listed above with the addition of the following variables:

- Dielectron
 - minimum of the likelihood, constructed from eight variables related to calorimeter shower shape and matching tracks, between the two electrons
 - number of Layer 0 hits for the minimum quality electron (Run IIb only)
 - number of Layer 0 hits for the maximum quality electron (Run IIb only)
- Electron-muon
 - electron likelihood constructed from eight variables related to calorimeter shower shape and matching tracks

- number of Layer 0 hits (Run IIb)
- muon quality
- Dimuon
 - minimum quality of the two muons
 - the track isolation of each muon

The following additional information is provided for the higher jet multiplicity bins (N_{jets}):

- Channels with $N_{\text{jets}} = 1$
 - $O(b\text{--tag})$: the output of a multivariate analysis trained to discriminate jets originating from b -quarks from those originating from light quarks.
- Channels with $N_{\text{jets}} > 1$
 - maximum $O(b\text{--tag})$
 - minimum $O(b\text{--tag})$
- All channels
 - the M_{T2} variable.
 - the product of charge and rapidity for ℓ_1
 - the product of charge and rapidity for ℓ_2

Simulated events are used to train the BDT to differentiate between all Higgs boson signal events, including gluon fusion, associated production and vector boson fusion, and all background events (diboson, $t\bar{t}$, W boson, Z/γ^* , etc.) in the three jet multiplicities (0, 1, and ≥ 2 jet bins), and for each Higgs boson mass considered. The BDT discriminant for the separate channels for a Higgs boson mass of 165 GeV can be found in Figures 6, 7 and 8. Before calculating limits, an additional requirement is applied in the ee and $\mu\mu$ channels to remove events from the zero jet bin for which the output of the BDT is less than -0.75. This is done to remove events from a signal-depleted region.

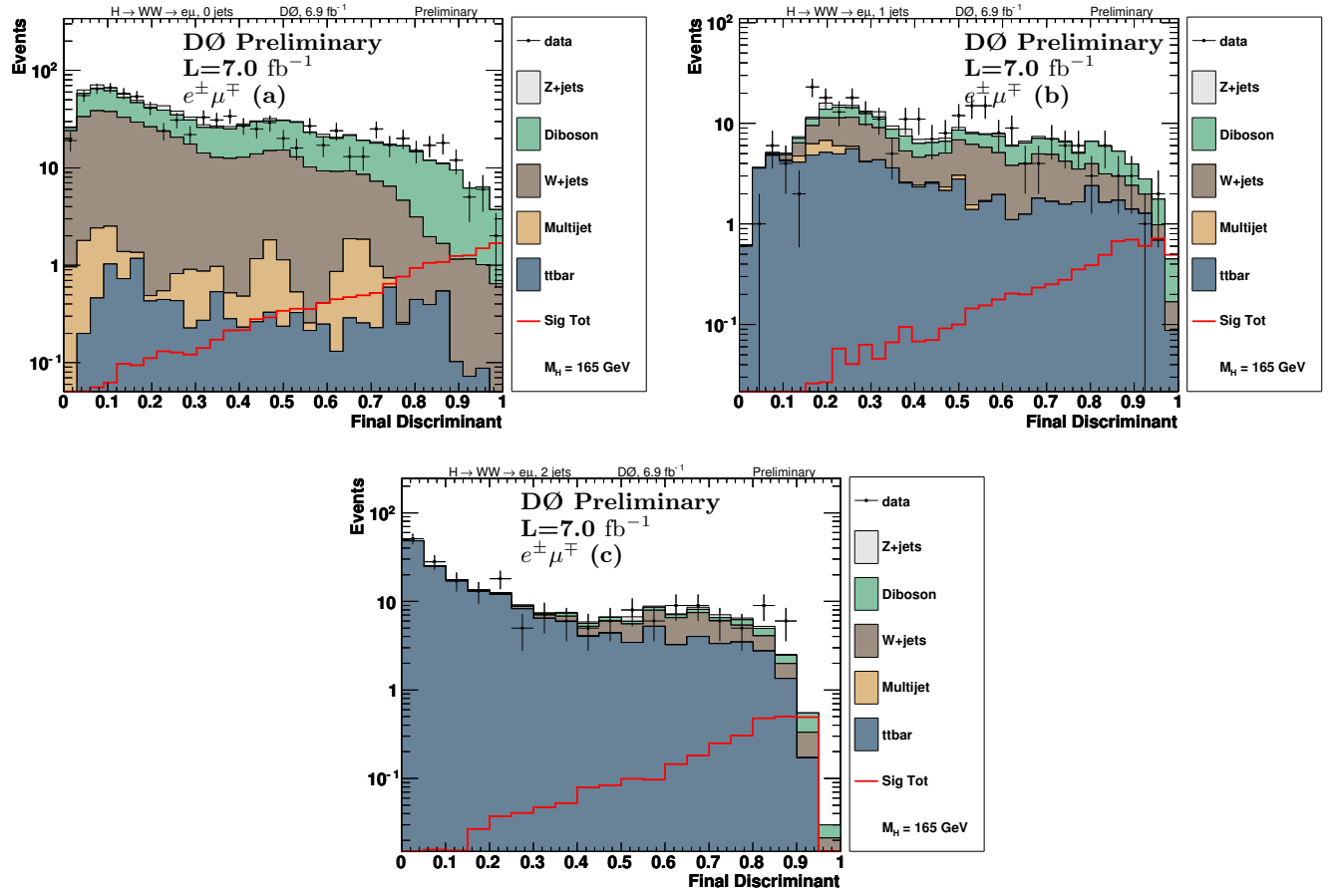


FIG. 6: Final BDT discriminant for $e\mu$ channel in (a) 0-jet bin, (b) 1-jet bin, (c) ≥ 2 -jet bin. The discriminant shown is trained for a Higgs mass of 165 GeV. These distributions correspond to the Run IIb dataset.

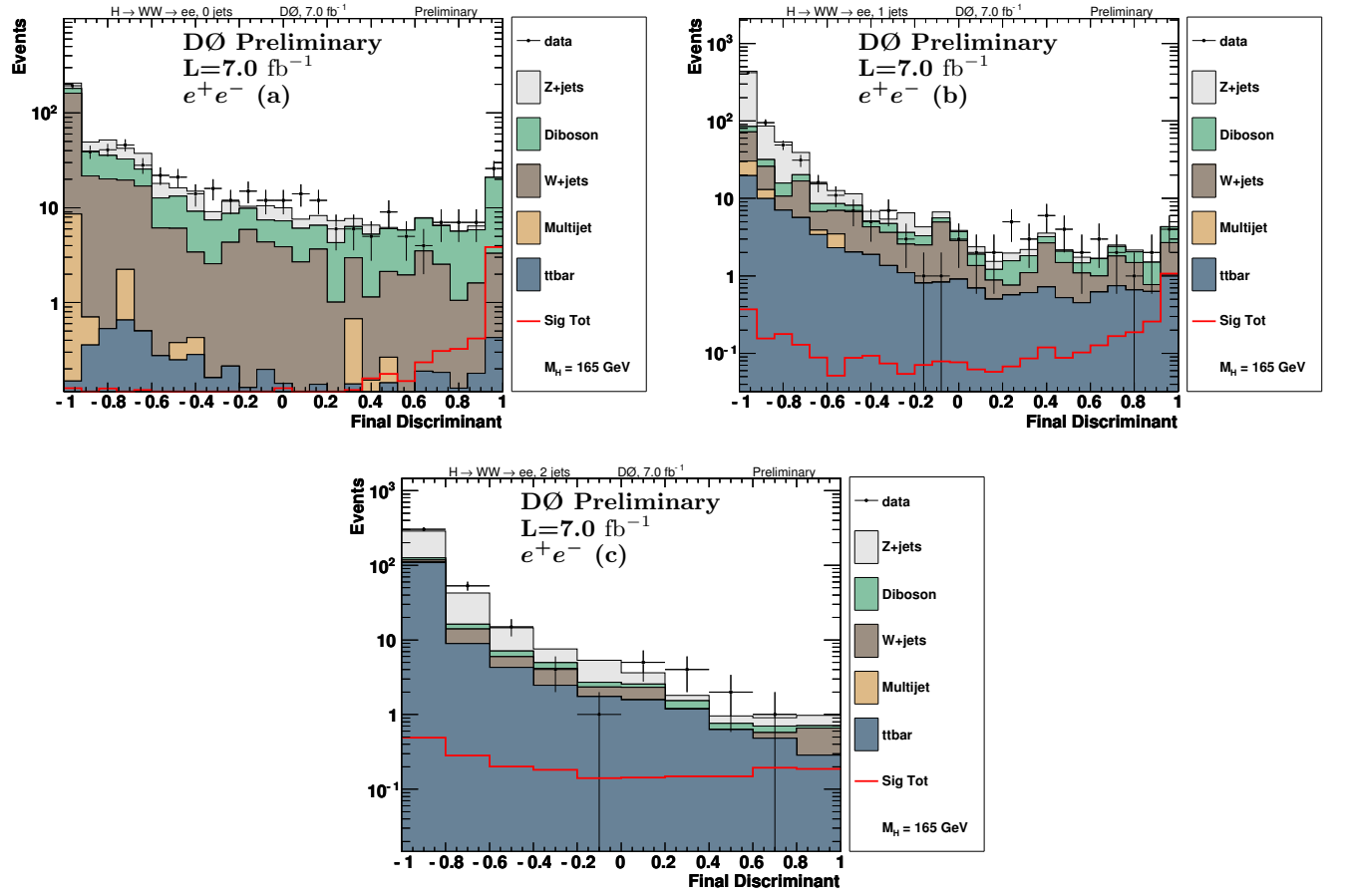


FIG. 7: Final BDT discriminant for ee channel in (a) 0-jet bin, (b) 1-jet bin, (c) ≥ 2 -jet bin. The discriminant shown is trained for a Higgs mass of 165 GeV. These distributions correspond to the Run IIb dataset.

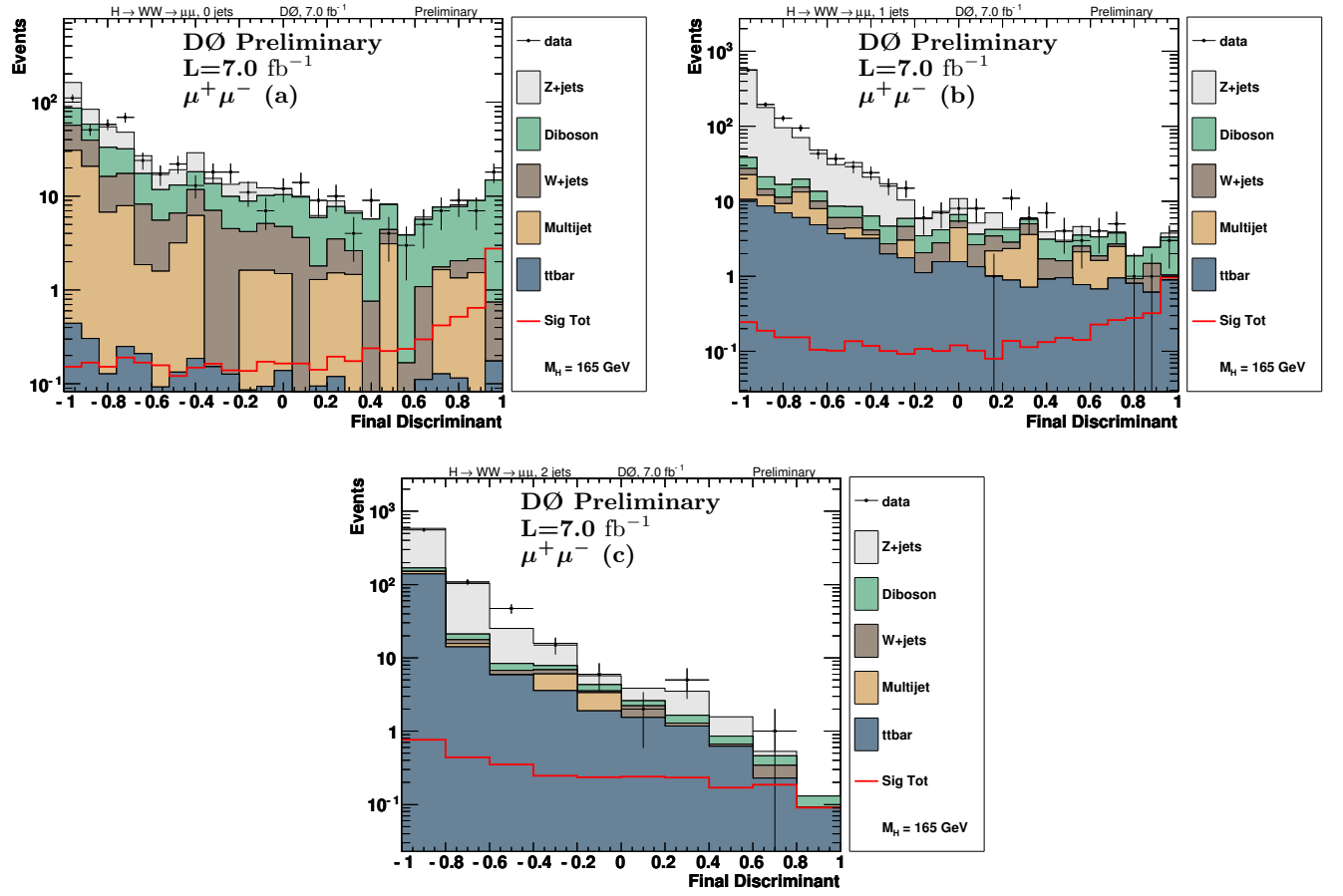


FIG. 8: Final BDT discriminant for $\mu\mu$ channel in (a) 0-jet bin, (b) 1-jet bin, (c) ≥ 2 -jet bin. The discriminant shown is trained for a Higgs mass of 165 GeV. These distributions correspond to the Run IIb dataset.

TABLE III: Expected and observed upper limits at 95% CL for $\sigma(p\bar{p} \rightarrow H + X)$ relative to the SM for the total combination and separately for the ee , $e\mu$ and $\mu\mu$ channels in Run II for different Higgs boson masses (M_H).

$M_H=$	115	120	125	130	135	140	145	150	155	160	165	170	175	180	185	190	195	200
Exp. all:	8.52	5.46	3.99	3.01	2.43	1.98	1.76	1.47	1.27	0.96	0.90	1.05	1.22	1.46	1.89	2.28	2.74	3.16
Obs. all:	9.54	8.18	7.14	4.59	3.55	3.01	3.10	2.05	1.92	1.22	0.78	1.10	1.59	1.88	2.02	2.47	2.86	3.62
Exp. $e\mu$:	13.54	8.02	5.74	4.41	3.67	2.93	2.64	2.23	1.95	1.44	1.31	1.53	1.79	2.22	2.73	3.40	3.91	4.78
Obs. $e\mu$:	21.34	12.77	13.72	7.74	5.76	4.52	3.66	2.67	2.10	1.21	1.10	1.68	1.98	2.79	3.00	3.91	3.83	4.73
Exp. ee :	18.97	13.25	9.22	7.01	5.44	4.55	3.90	3.37	2.84	2.18	2.08	2.28	2.78	3.26	4.10	5.04	6.05	6.77
Obs. ee :	12.20	13.69	8.36	8.54	5.72	6.41	6.06	4.39	4.58	3.23	2.62	2.96	3.42	3.13	4.09	4.74	6.17	7.62
Exp. $\mu\mu$:	19.09	13.15	9.28	6.71	5.49	4.41	3.87	3.37	2.78	2.17	2.18	2.60	2.96	3.50	4.56	5.30	6.41	7.39
Obs. $\mu\mu$:	26.09	15.95	11.13	7.77	7.02	6.05	7.17	5.06	4.66	3.60	2.15	2.47	4.35	4.69	5.58	5.71	8.89	10.29

VII. RESULTS AND SUMMARY

The sources of systematic uncertainties that affect only the normalization are: reconstruction efficiency for electrons (2.5% each) and muons (4% each); electron resolution (2% each); theoretical cross sections for Z +jets (6%), W +jets (6%), diboson (7%), and $t\bar{t}$ (10%); multijet normalization (20%); W +jets overall normalization (20%); b -tagging in the heavy-flavor $t\bar{t}$ sample (5%) and remaining light-flavor samples (10%); luminosity/normalization (6%); and a Z +jets jet bin dependent normalization ((2–15)%). The signal $gg \rightarrow H$ cross-section has different scale and PDF uncertainties depending on the reconstructed jet bin. Using the prescription described in [27], the $gg \rightarrow H$ cross-section scale/PDF uncertainties range between (13-33)%/(7.6-30)%, depending on the jet bin. We also consider sources of systematic uncertainty which affect the shape of the final discriminant distribution (and quote here the average fractional change across bins of the final discriminant distribution for all backgrounds): jet energy scale (2.4%); jet resolution (3.8%); jet identification (2.1%); jet association to primary vertex (vertex confirmation) (1.7%). Several systematics are included which have a small ($< 1\%$) effect on the background model: modeling of diboson production in terms of $p_T(WW)$ and $\Delta\phi$ between the leptons, and the p_T of the vector boson from W +jets and Z +jets production. The shape change due to PDF uncertainties was found to be small and a flat 2.5% systematic was instead applied to all background MC samples.

The BDT output distributions in data agree within uncertainties with the expected backgrounds as shown in Figures 6, 7 and 8. The BDT output distributions are therefore used to set limits on the Higgs boson inclusive production cross section $\sigma(p\bar{p} \rightarrow H + X)$ assuming SM values for the branching ratios and for the relative cross sections of the various Higgs production mechanisms considered. We calculate limits using a modified frequentist method (CLs), with a log-likelihood ratio (LLR) test statistic [28]. All lepton channels are combined in the limit, but to achieve maximal sensitivity, the 18 individual inputs (3 leptonic channels, 3 jet bins, and 2 data taking periods Run IIa and Run IIb) are treated separately by the limit setting software. To minimize the degrading effects of systematics on the search sensitivity, the individual background contributions are fitted to the data observation by maximizing a profile likelihood function for the background-only and signal-plus-background hypotheses [29].

Table III presents expected and observed upper limits at 95% CL for $\sigma(p\bar{p} \rightarrow H + X)$ relative to that expected in the SM for each Higgs boson mass considered. Figure 9 shows the expected and observed limits for $\sigma(p\bar{p} \rightarrow H + X)$ relative to the SM for the different Higgs boson masses, while Figure 10 shows the corresponding LLR distribution. At $M_H = 165$ GeV, the observed limit ratio is 0.91, with 0.97 expected, indicating that a standard model Higgs boson of this mass is excluded at the 95% CL. While this region is already excluded by the Tevatron combination since 2010 [30], it is remarkable that this is achieved analysing only one single Higgs boson decay mode, i.e. the $H \rightarrow WW$ decay process.

VIII. FOURTH GENERATION INTERPRETATION

The cross section limit of the $gg \rightarrow H \rightarrow VV$ ($V = Z, W$) process is interpreted under the assumption of a fourth generation of fermions. Additional generations of fermions can occur naturally in models of grand unification, CP violation, gauge-mediated supersymmetry breaking and others. While measurements of the Z boson decay width [33] exclude models in which the fourth neutrino mass eigenstate is lighter than 45 GeV, fourth generation models can still be accommodated for a very large fourth generation neutrino mass. A heavy fourth SM family of quarks leads to a significant enhancement of the $gg \rightarrow H$ production cross-section arising from contributions to the quark loop. The enhancement factor is a function of the masses of the fourth generation quarks and the smallest enhancement is predicted in the limit of infinite fourth generation quark masses. This is due to the cancellation between the Higgs boson coupling and the mass dependence for each of the three propagators in the loop. The enhancement

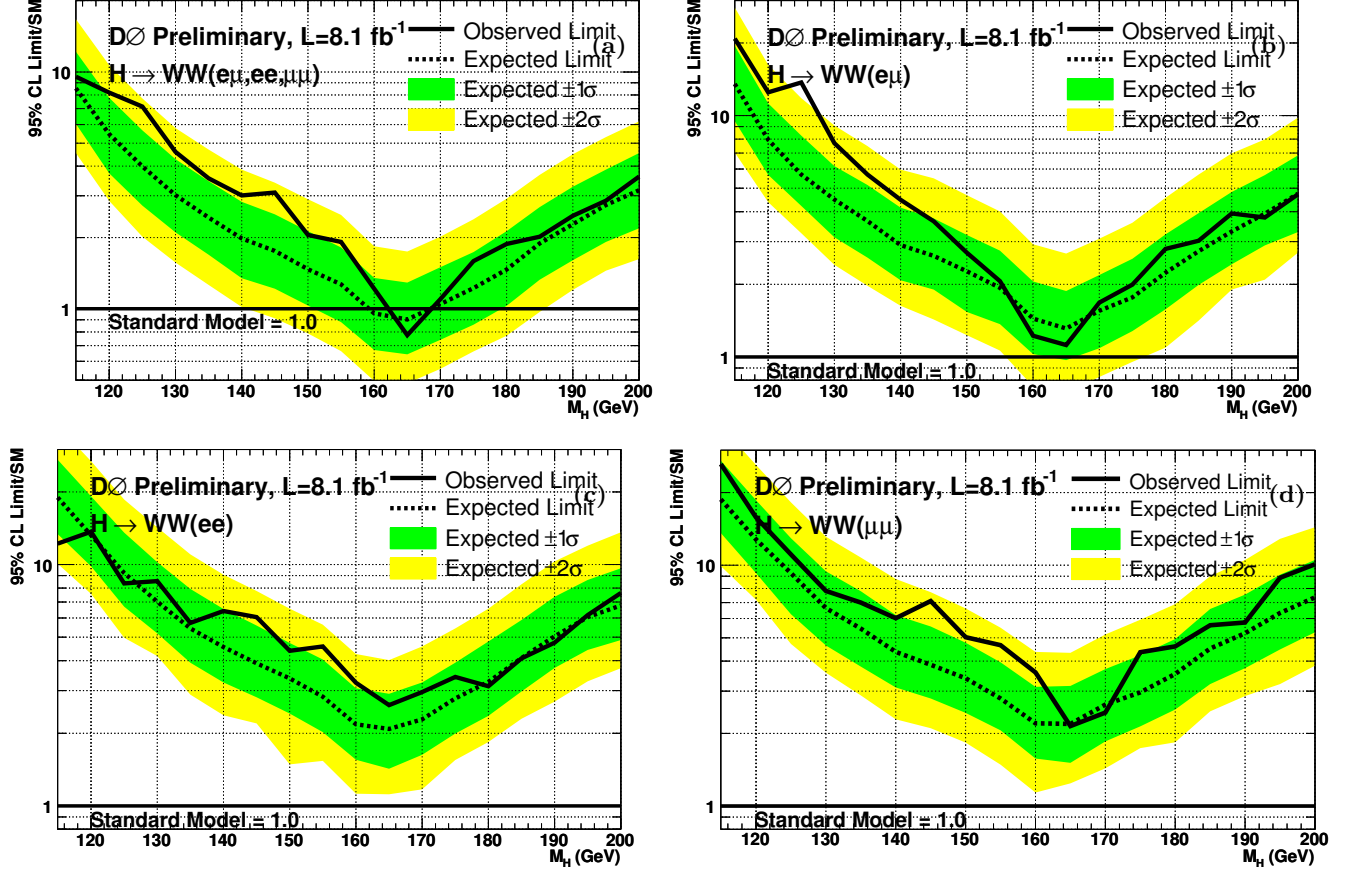


FIG. 9: Excluded cross section ($\sigma(p\bar{p} \rightarrow H + X)$) at 95% CL in units of the SM cross section as a function of M_H using (a) all channels, (b) $e\mu$ channel, (c) ee channel, (d) $\mu\mu$ channel.

varies roughly between a factor of 9 and 7 depending on the fourth generation quark masses and the Higgs mass [34][35][36]. We consider the production of the Higgs boson only via gluon fusion in two models, depending on the fourth generation charged lepton (ℓ_4) and neutrino (ν_4) masses. The “low-mass” scenario considers $m_{\ell_4} = 100$ GeV and $m_{\nu_4} = 80$ GeV where both masses are just beyond the experimental limits and have a maximum impact on the Higgs boson branching ratios, and the “high-mass” scenario where $m_{\ell_4} = m_{\nu_4} = 1$ TeV and are too heavy to contribute to Higgs boson decays. For both scenarios the masses of the fourth-generation down-type (m_{d_4}) and up-type (m_{u_4}) quarks are fixed to $m_{d_4} = 400$ GeV and $m_{u_4} = 450$ GeV [35][34].

A previous combined DØ and CDF search using up to 5.4 fb^{-1} excluded the presence of a standard model like Higgs boson, in the presence of a fourth sequential generation of fermions with large masses, in the mass range between 131 and 204 GeV at 95% confidence [37].

An updated analysis is carried out using 8.1 fb^{-1} of DØ data using the analysis strategy described in sections IV-VI but with two adjustments.

1. The DY and Final BDT discriminants are both re-trained only considering the gluon fusion production as signal,
2. Due to the low S/B in the ≥ 2 -jet multiplicity bin, only the 0 and 1-jet multiplicity bins were taken into account.

The Final BDT discriminant for the separate channels for a SM Higgs boson with a mass of 165 GeV is shown in Figure 11. Using these distributions a limit is set on $\sigma(gg \rightarrow H) \times BR(H \rightarrow WW)$. The cross section limit is independent of the theoretical prediction of the signal process and therefore independent of theoretical uncertainties. Figure 12, and Table IV show the $\sigma(gg \rightarrow H) \times BR(H \rightarrow WW)$ limit for the three individual channels and their combination. Assuming the presence of a fourth generation of fermions with large masses, an exclusion range of M_H between 140 GeV and 240 GeV at 95% CL is obtained using 8.1 fb^{-1} of integrated luminosity.

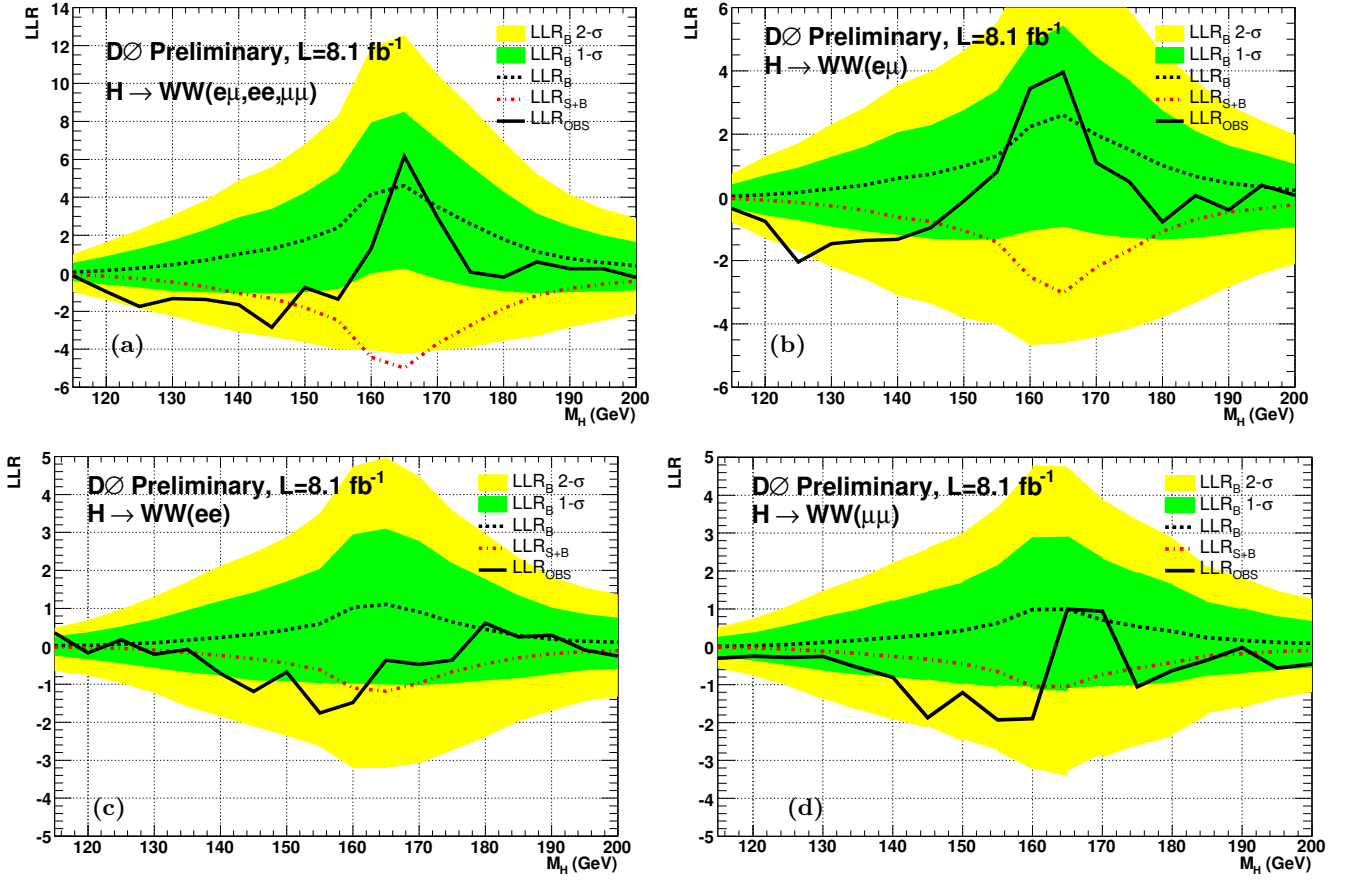


FIG. 10: The observed LLR (solid line) as a function of M_H using (a) all channels, (b) $e\mu$ channel, (c) ee channel, (d) $\mu\mu$ channel. Also shown are the expected LLRs for the B (black dashed line) and S+B (red dashed line) hypotheses, with the green and yellow bands indicating one and two sigma fluctuations of the expected LLR for the B -only hypothesis.

IX. CONCLUSIONS

A search for the standard model Higgs boson in dilepton ($e^\pm\mu^\mp$, e^+e^- , $\mu^+\mu^-$) events with large missing transverse energy using 8.1 fb^{-1} of $p\bar{p}$ collisions at $\sqrt{s} = 1.96 \text{ TeV}$, collected with the DØ detector at the Fermilab Tevatron collider was presented. No significant excess above the standard model background expectation was observed, and upper limits on Higgs boson production were derived. Using this channel alone, a standard model Higgs boson with a mass of $M_H=165 \text{ GeV}$ was excluded at 95% CL. Assuming the presence of a fourth generation of fermions with large masses, a SM-like Higgs with a mass between 140 and 240 GeV was excluded.

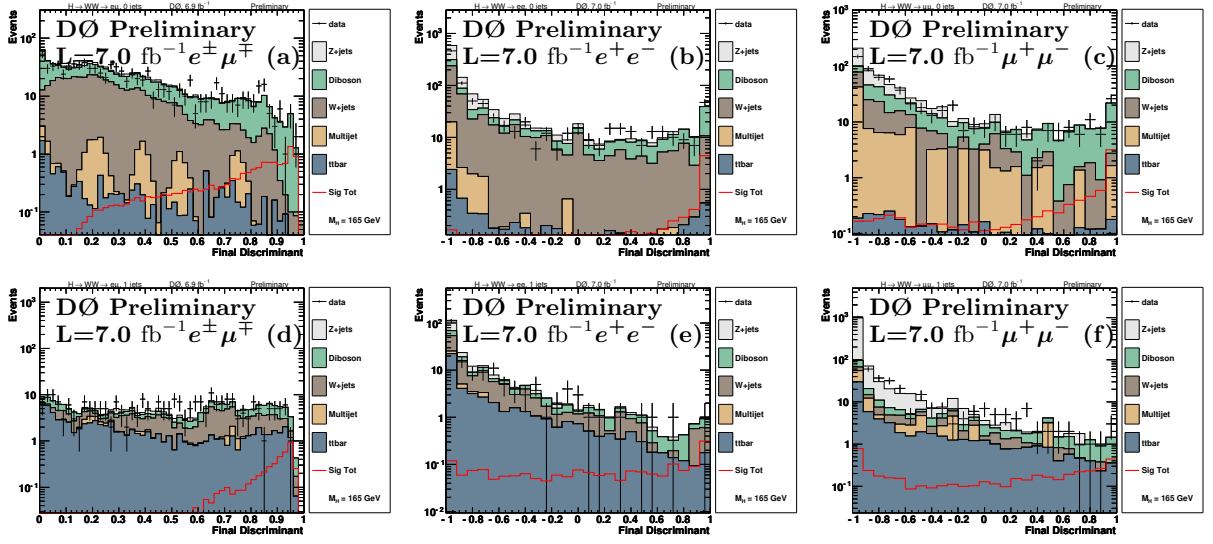


FIG. 11: Final BDT discriminant for the $e\mu$ channel (left column), the ee channel (middle column) and the $\mu\mu$ channel (right column). Figures (a)-(c) represent the 0-jet bin, and (d)-(f) the 1-jet bin. The discriminant shown is trained for a gluon fusion produced Higgs with a mass of 165 GeV. These distributions correspond to the Run IIb dataset.

TABLE IV: Expected and observed upper limits at 95% CL for $\sigma(gg \rightarrow H) \times BR(H \rightarrow WW)$ in pb for the total combination and separately for the ee , $e\mu$ and $\mu\mu$ channels in Run II for different Higgs boson masses (M_H).

$M_H =$	115	120	125	130	135	140	145	150	155	160	165	170	175	180
Exp. all:	1.19	1.12	1.06	1.02	0.96	0.89	0.81	0.73	0.63	0.46	0.41	0.44	0.49	0.52
Obs. all:	1.64	1.70	1.99	2.22	2.02	2.11	1.53	1.21	1.23	0.76	0.61	0.48	0.55	0.75
Exp. $e\mu$:	1.86	1.48	1.37	1.30	1.24	1.17	1.11	0.97	0.86	0.63	0.57	0.62	0.66	0.71
Obs. $e\mu$:	1.97	2.54	3.09	3.15	2.60	2.38	1.47	1.31	1.05	0.81	0.62	0.71	0.73	0.81
Exp. ee :	2.72	2.41	2.40	2.14	2.02	1.74	1.64	1.48	1.31	0.97	0.89	0.91	0.95	1.12
Obs. ee :	2.77	2.18	2.51	2.41	2.24	1.83	2.21	1.43	2.31	1.34	1.46	0.96	1.28	1.47
Exp. $\mu\mu$:	2.22	2.23	2.05	2.00	1.81	1.81	1.49	1.42	1.14	0.92	0.80	0.90	1.08	1.07
Obs. $\mu\mu$:	3.38	2.83	2.34	2.84	2.61	3.34	2.40	2.27	1.71	1.59	1.20	1.10	1.07	1.31
$M_H =$	185	190	195	200	210	220	230	240	250	260	270	280	290	300
Exp. all:	0.54	0.57	0.62	0.66	0.67	0.68	0.60	0.61	0.57	0.57	0.57	0.56	0.54	0.54
Obs. all:	0.77	0.69	0.60	0.59	0.49	0.60	0.47	0.52	0.52	0.42	0.50	0.46	0.59	0.42
Exp. $e\mu$:	0.73	0.76	0.80	0.85	0.83	0.86	0.87	0.89	0.85	0.86	0.81	0.78	0.75	0.76
Obs. $e\mu$:	0.74	0.79	0.80	0.77	0.59	0.54	0.58	0.62	0.50	0.57	0.55	0.68	0.72	0.58
Exp. ee :	1.15	1.13	1.29	1.32	1.49	1.49	1.30	1.22	1.07	1.07	1.07	1.08	1.03	0.99
Obs. ee :	1.74	1.46	1.05	1.21	1.22	1.67	1.20	1.17	1.02	0.54	0.62	0.65	0.65	0.54
Exp. $\mu\mu$:	1.13	1.18	1.28	1.38	1.61	1.39	1.10	1.13	1.08	1.17	1.26	1.24	1.32	1.23
Obs. $\mu\mu$:	1.42	1.07	1.26	1.35	1.81	1.89	1.15	1.21	1.26	1.76	2.06	1.41	2.32	1.68

- [1] R. Barate *et al.*, Phys. Lett. B **565**, 61 (2003).
- [2] The TEVNPH Working Group, arXiv:1103.3233v2 [hep-ex]
- [3] The LEP Electroweak Working Group, the Tevatron Electroweak Working Group, *Precision Electroweak Measurements and Constraints on the Standard Model*, arXiv:1012.2367 [hep-ex].
- [4] V. M. Abazov *et al.*, Phys. Rev. Lett. **104**, 061804 (2010).
- [5] DØ Collaboration, V. Abazov *et al.*, Nucl. Instrum. Methods Phys. Res. A. **565**, 463 (2006).
- [6] T. Andeen *et al.*, Report. No. FERMILAB-TM-2365 (2007).
- [7] T. Sjöstrand *et al.*, Comp. Phys. Comm. **135**, 238 (2001), we use version 6.323 or later.
- [8] M.L. Mangano, M. Moretti, F. Piccinini, R. Pittau, A. Polosa, JHEP **0307**, 001 (2003), we use version 2.11.
- [9] J. Pumplin *et al.*, JHEP **07**, 012 (2002).
- [10] R. Brun and F. Carminati, CERN Program Library Long Writeup W5013, 1993 (unpublished).

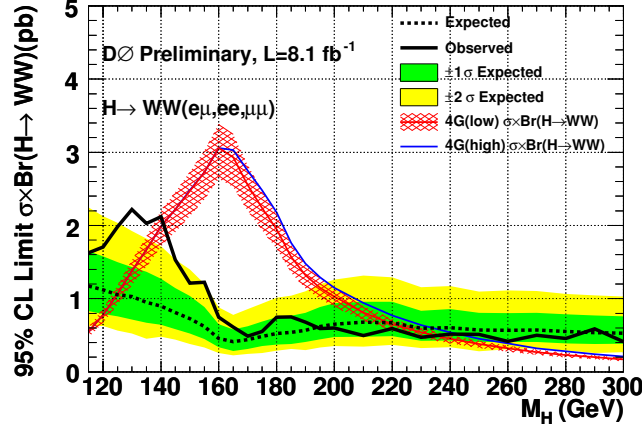


FIG. 12: (a) Excluded $\sigma(gg \rightarrow H) \times BR(H \rightarrow WW)$ at 95% CL in pb as a function of M_H using all channels. The red and blue lines corresponds to the theoretical prediction for a sequential fourth generation assumption in the “low mass” and “high mass” scenarios respectively. The red shaded region corresponds to the PDF and scale uncertainties on the fourth generation “low mass” prediction [34].

- [11] D. Florian and M. Grazzini, Phys. Lett. B **674** 291-294 (2009).
- [12] J. Baglio and A. Djouadi, arXiv:1003.4266v2 [hep-ph].
- [13] P. Bolzoni *et al.*, arXiv:1003.4451v2 [hep-ph]
- [14] A. D. Martin, W. J. Stirling, R. S. Thorne and G. Watt, Eur. Phys. J. **C63**, 189 (2009) [arXiv:0901.0002 [hep-ph]]
- [15] S. Alekhin *et al.*, arXiv:1101.0536v1 [hep-ph]; M. Botje *et al.*, arXiv:1101.0538v1 [hep-ph].
- [16] G. Bozzi, S. Catani, D. de Florian, M. Grazzini, Phys. Lett. B **564** (2003) 65 [hep-ph/0302104]; Nucl. Phys. B **737** (2006) 73 [hep-ph/0508068].
- [17] R. Hamberg, W.L. van Neerven, and T. Matsuura, Nucl. Phys. **B359**, 343 (1991) [Erratum-ibid. **B644**, 403 (2002)].
- [18] DØ Collaboration, V. Abazov *et al.*, Phys. Rev. Lett. **100**, 102002 (2008)
- [19] K. Melnikov and F. Petriello, Phys. Rev. D **74**, 114017 (2006).
- [20] S. Moch, P. Uwer, Phys. Rev. D **78**, 034003 (2008), we use $\sigma(t\bar{t}) = 7.88$ pb.
- [21] J. M. Campbell and R. K. Ellis, Phys. Rev. D **60**, 113006 (1999), we use $\sigma(WW) = 11.66$ pb, $\sigma(WZ) = 3.45$ pb and $\sigma(ZZ) = 1.37$ pb.
- [22] S. Frixione and B.R. Webber, JHEP **0206** (2002) 029 [hep-ph/0204244].
- [23] T. Binoth, M. Ciccoli, N. Kauer, M. Krämer, JHEP **0503**, 065 (2005), JHEP **0612**, 046 (2006).
- [24] G.C. Blazey *et al.*, [hep-ex/0005012] (2000)
- [25] V.M. Abazov *et al.*, (DØ Collaboration), Phys. Rev. Lett. **101**, 062001 (2008).
- [26] C.G. Lester, D.J. Summers, Phys. Lett. **B463**, 99-103, (1999); H. Cheng, Z. Han, JHEP **12**, 063 (2008).
- [27] V.M. Abazov *et al.*, (DØ collaboration), DØ Conference Note 6229.
- [28] T. Junk, Nucl. Instrum. Methods Phys. Res. A. **434**, 435 (1999). A. Read, CERN 2000-005 (30 May 2000).
- [29] W. Fisher, FERMILAB-TM-2386-E.
- [30] T. Aaltonen *et al.*, (CDF and DØ Collaborations), Phys. Rev. Lett. **104**, 061802 (2010).
- [31] C. Anastasiou, G. Dissertori, M. Grazzini, F. Stöckli and B. R. Webber, JHEP **0908**, 099 (2009), arXiv:0905.3529 [hep-ph].
- [32] J. M. Campbell, R. K. Ellis, C. Williams, Phys. Rev. **D81**, 074023 (2010), arXiv:1001.4495 [hep-ph].
- [33] ALEPH, DELPHI, L3, OPAL, SLD Collaborations, LEP Electroweak Working Group, and SLD Electroweak and Heavy Flavor Groups, Phys. Rep. **427**, 257 (2006).
- [34] C. Anastasiou, R. Boughezal, and E. Furlan, arXiv:1003.4677 [hep-ph].
- [35] G. D. Kribs, T. Plehn, M. Spannowsky, and T. M. P. Tait, Phys. Rev. **D76**, 075016 (2007), arXiv:0706.3718v1 [hep-ph].
- [36] E. Arik, O. Cakir, S. A. Cetin, and S. Sultansoy, Acta Phys. Polon. **B37**, 2839 (2006), arXiv:hep-ph/0502050v6.
- [37] T. Aaltonen *et al.* (CDF Collaboration, DØ Collaboration) Phys. Rev. D **82**, 011102 (2010).